



**HAL**  
open science

## Reducing parasitic effects of actuation and sensing schemes for piezoelectric microelectromechanical resonators

Fabrice Mathieu, Florian Larramendy, Denis Dezest, C. Huang, G. Lavallée, S. Miller, C.M. Eichfeld, W. Mansfield, S. Trolier-Mckinstry, Liviu Nicu

► **To cite this version:**

Fabrice Mathieu, Florian Larramendy, Denis Dezest, C. Huang, G. Lavallée, et al.. Reducing parasitic effects of actuation and sensing schemes for piezoelectric microelectromechanical resonators. *Microelectronic Engineering*, 2013, 111, pp. 68-76. hal-00797039

**HAL Id: hal-00797039**

**<https://hal.science/hal-00797039>**

Submitted on 5 Mar 2013

**HAL** is a multi-disciplinary open access archive for the deposit and dissemination of scientific research documents, whether they are published or not. The documents may come from teaching and research institutions in France or abroad, or from public or private research centers.

L'archive ouverte pluridisciplinaire **HAL**, est destinée au dépôt et à la diffusion de documents scientifiques de niveau recherche, publiés ou non, émanant des établissements d'enseignement et de recherche français ou étrangers, des laboratoires publics ou privés.

1           **Reducing parasitic effects of actuation and sensing schemes for**  
2           **piezoelectric microelectromechanical resonators**

3           F. Mathieu,<sup>1,2</sup> F. Larramendy,<sup>1,2</sup> D. Dezest,<sup>1,2</sup> C. Huang,<sup>3</sup> G. Lavallee,<sup>3</sup> S. Miller,<sup>3</sup> C. M.  
4           Eichfeld,<sup>3</sup> W. Mansfield,<sup>3</sup> S. Trolier-McKinstry,<sup>3</sup> and L. Nicu<sup>1,2</sup>

5           <sup>1</sup> CNRS, LAAS, 7 avenue du Colonel roche, F-31400, Toulouse, France

6           <sup>2</sup> Univ de Toulouse, LAAS, F-31400 Toulouse, France

7           <sup>3</sup> Nanofabrication Laboratory, Materials Research Institute, The Pennsylvania State University

8  
9           **Abstract**

10           The co-integration of piezoelectric actuation and sensing capabilities on  
11           microelectromechanical system-based resonators can be a source of electrical cross-talk that, if not  
12           properly taken into account, may dramatically affect the interpretation of the device's output. In this  
13           paper, we identify three parasitic electrical effects pertaining to the most commonly used piezoelectric  
14           actuation and sensing schemes. **To further investigate the impact of such parasitic effects,**  
15           microcantilevers, bridges and membranes integrating a layer of sol-gel lead zirconate titanate (PZT)  
16           were fabricated and electrically characterized. Experimental results on the resonant characteristics  
17           were compared with simulations of the studied resonators' equivalent electrical models. Methods for  
18           reducing the design-dependent parasitic electrical effects such as mutual capacitances of less than  
19           10fF, electrical wiring or static capacitance mismatches of less than 20% of the integrated  
20           piezoelectric films are discussed.

21

22

## 23 Introduction

24 Piezoelectric materials enable high performance actuator and sensor systems satisfying  
25 dimensional integration constraints from the millimeter to the micrometer scale [1-3]. Piezoelectricity  
26 is appealing for electromechanical transduction as it allows energy conversion from the mechanical to  
27 the electrical domain and vice-versa. Extensive reports are available on the challenges associated with  
28 the integration of such materials at the microscale, as well as the direct impact of miniaturization and  
29 dimensionality on the electromechanical properties of the resulting devices [4-8]. Starting from H.  
30 Tilmans work [9] that laid the foundations for developing equivalent electrical circuits of electro-  
31 mechanical transducers and their interconnection to the outside world, Studies [10-13] where lumped  
32 element-based modeling is used to predict the behavior of multiphysics microsensors integrating  
33 piezoelectric active layers have been carried out. Nonetheless, the provided solutions are most of time  
34 application-dependent. Such dependence dramatically constraints the generic aim of the proposed  
35 models. In this paper, we propose a simplified electrical modeling of the chip hosting piezoelectric  
36 resonators presenting conventional geometries (cantilever, bridge and membrane) and the way in  
37 which the “electrical environment” of such integrated resonators may influence their performance.

38 In the following, a piezoelectric material sandwiched between two metallic electrodes will be  
39 called a *piezo-cell* and a microdevice integrating piezo-cells for actuation and/or sensing purposes as  
40 well as the contacting wires will be called a *piezo-device*. To address the holistic electrical modeling of  
41 piezoelectric MEMS, one has to hierarchically answer three questions:

- 42 (1) The **piezo-cell** level: is there a generic way to electrically model a piezo-cell taking into  
43 account the influence of the associated parasitic “on chip-electrical wiring”?
- 44 (2) The **piezo-device** level: is there an ideal actuation/sensing element topology that minimizes  
45 the influence of the parasitic capacitances?
- 46 (3) The **system** level: based upon the answers to (1) and (2), is it possible to devise specific  
47 sensing electronics that effectively interface to the piezoelectric devices?

48 The on-chip actuation and sensing schemes studied in this paper along with the use of dedicated  
49 electronics developed for this purpose aim to answer these questions. A series of design rules for  
50 piezoelectric materials integration is proposed from the standpoint of MEMS-based resonator  
51 development.

52

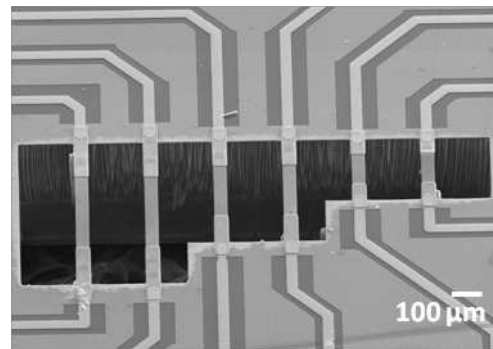
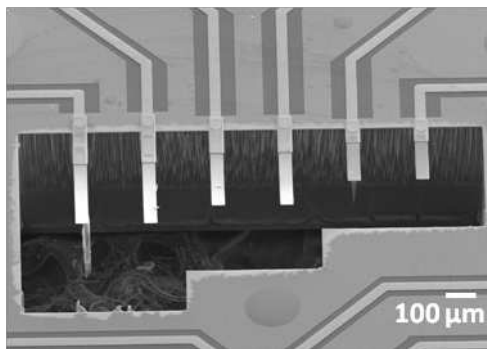
### 53 **Device Fabrication**

54 The fabrication process for the MEMS resonators is depicted in Fig. S1 (see Supplementary  
55 Information file). A double-side polished silicon-on-insulator (SOI) wafer with a 2  $\mu\text{m}$  Si device layer  
56 and a 1  $\mu\text{m}$  buried oxide layer was used as the starting substrate. The mask set for the wafer hosts chips  
57 bearing cantilevers, bridges and membranes. The cantilevers and bridges are 50- $\mu\text{m}$  wide and paired,  
58 with lengths of 300  $\mu\text{m}$ , 500  $\mu\text{m}$  or 700  $\mu\text{m}$ . The piezoelectric layer covers one quarter of the full length  
59 of the cantilevers, beginning at the clamping point to the substrate and one eighth of the bridge length at  
60 each of the ends. The membranes are circular with diameters of 50 $\mu\text{m}$ , 200  $\mu\text{m}$  or 450  $\mu\text{m}$ . The  
61 piezoelectric layer covers two distinct regions on each membrane: an inner full circle with a diameter  
62 that is half the full membrane diameter, and an outer ring-like area with a width that is 0.25 of the  
63 membrane's diameter.

64 To fabricate these devices, the first step was the growth of a 100-nm-thick thermal silicon dioxide  
65 film on the SOI wafer. A metal-complex oxide-metal sandwich structure was then deposited on the  
66 thermal  $\text{SiO}_2$ . A bottom electrode consisting of a 20 nm titanium adhesion layer and 100nm platinum of  
67 Pt was then deposited. A 1.6  $\mu\text{m}$  layer of lead zirconate titanate (PZT:  $\text{Pb}(\text{Zr}_{0.52}\text{Ti}_{0.48})\text{O}_3$ ) was then spin  
68 deposited from a sol gel solution on the bottom electrode as described elsewhere [14]. Finally, a top  
69 electrode of 100nm of platinum was sputter deposited on the PZT. Subsequent lithography defined the  
70 active device structure. The active device pattern was transferred to the top electrode (100nm Pt) and  
71 the 1.6  $\mu\text{m}$  PZT layer by dry etching using a thick resist as a mask (Shipley SPR220). The dry etch  
72 process was run in a Tegal 6540 HRe<sup>-</sup> capacitively coupled plasma chamber using a mixture of  $\text{Cl}_2$  and  
73  $\text{CF}_4$  gases and a process pressure of  $\sim 5$  mTorr. The PZT etch was stopped on the bottom platinum

74 electrode. A second set of lithography and plasma etch steps were used to define the bottom electrode  
75 patterns. A 400-nm-thick isolation film of silicon dioxide was then sputter deposited to avoid possible  
76 hydrogen damage of the PZT piezoelectric layer. Contact lithography and inductively coupled plasma  
77 (ICP) oxide etch processes were then used to open contacts to both top and bottom electrodes. The  
78 interconnect traces and pads were formed by a liftoff process of an electron beam-evaporated Ti/Au  
79 (10/150 nm) metal onto an undercut bi-level resist structure. A separate lithography step was then  
80 utilized to define the cantilever device structures; the isolation oxide, device silicon and buried oxide  
81 was etched using ICP etch processes (in a PlasmaTherm Versalock cluster tool) to form the beam  
82 structures. The cantilever and membrane devices were released utilizing backside thick resist  
83 lithography and Bosch etching through the handle wafer. The etching was stopped on the SOI buried  
84 oxide layer. During this step, the front-side structures were protected with a thick resist layer. After the  
85 handle wafer etch, the protection resist was removed to release both cantilever structures and membrane  
86 structures and the device chips were gently extracted from the wafer by applying pressure with tweezers  
87 at the separating paths running through the wafer.

88 Scanning electron microscope (SEM) images of micromachined cantilevers, bridges and  
89 membrane devices are shown in Figure 1. Following fabrication, the cantilevers exhibit out-of-plane  
90 static deflection as a result of global tensile stresses specific to the multilayer sandwich structure of the  
91 devices.

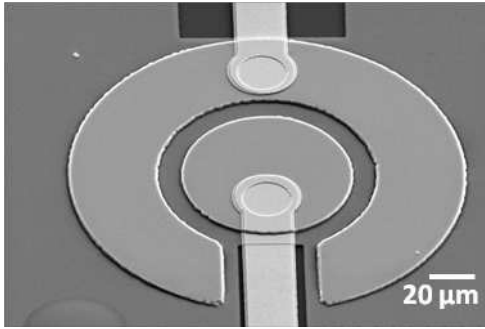


92

93

(a)

(b)



94

95

(c)

96

Figure 1: SEM images of micromachined (a) cantilevers, (b) bridges and (c) membrane devices.

97

98

99

Figure S2 (Supplementary Information file) shows the layout of the cantilevers/bridges and membranes chips as well as the identification of the different actuation/sensing piezoelectric areas corresponding to each device.

100

### Electrical modeling of a generic piezo-cell

101

102

103

104

105

106

107

The integration of piezoelectric thin films for different MEMS applications is commonly performed on metalized silicon substrates. Typical doping levels of such substrates (even at low values, i.e.  $10^{13}$  dopant atoms/cm<sup>3</sup>) render them rather conductive when compared to ceramic substrates. To electrically isolate piezo-cells from the underlying silicon substrate, one generally grows silicon dioxide onto the substrate prior to the piezo-cell patterning. This SiO<sub>2</sub> (or ZrO<sub>2</sub>, HfO<sub>2</sub>, etc.) layer also serves to minimize reactions between Pt metallization and the Si at typical process temperatures for perovskite piezoelectrics.

108

109

110

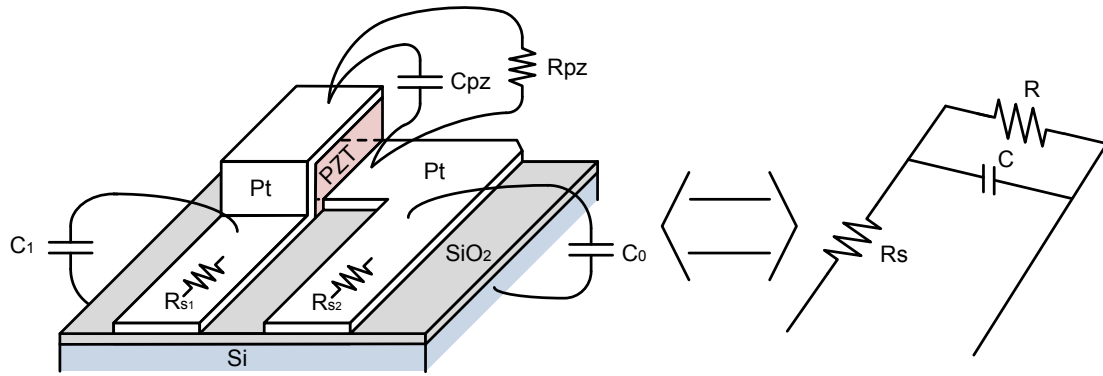
111

112

113

In order to model a simple equivalent electrical circuit, we proceed to a  $R_p$ - $C_p$  base transformation of the gain-phase measurement and subsequently identify the equivalent  $R_s$ ,  $C$  and  $R$  values (where  $R_s$  is the series resistance of the electrical wiring while  $C$  and  $R$  are respectively the capacitance and resistance of the piezo-device including  $R_{pz}$  – piezocell's resistance and  $C_{pz}$  – piezocell's capacitance), as depicted in Figure 2(a).

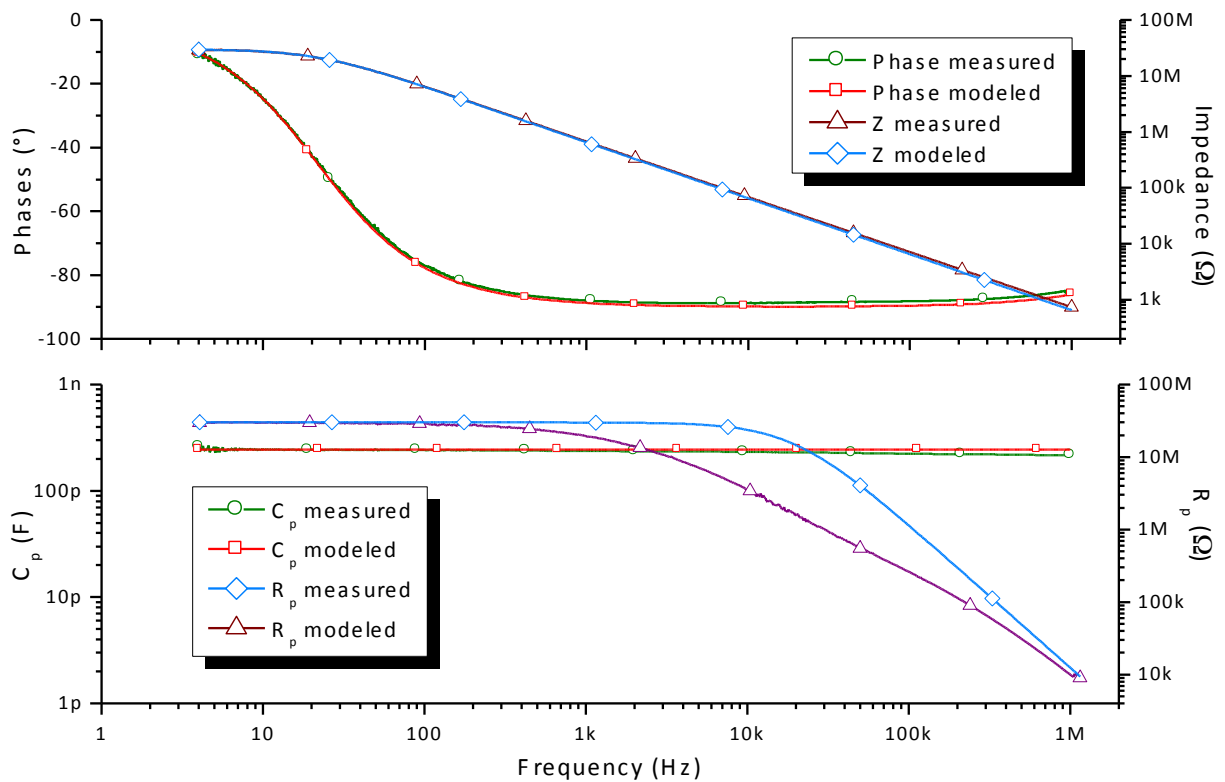
114 The  $R_p$  and  $C_p$  values are respectively given by  $R_p = \frac{|Z|}{\cos\theta}$  and  $C_p = \frac{-\sin\theta}{|Z|\omega}$  whereas the impedance  
 115  $Z = R_s + \frac{R}{1+jRC\omega}$ . Figure 2.(b) compares the measured and modeled data using the extracted  
 116 parameters for a S1<sub>i</sub> circular piezo-cell.



117

118

(a)



119

120

(b)

121 **Figure 2:** (a) Equivalent circuit of a piezo-device; (b) Gain-phase and corresponding  $R_p$ - $C_p$  frequency  
 122 responses of a  $S1_i$  circular piezo-cell. The graphs include both measured responses (green and blue  
 123 colored) and corresponding theoretical fit (red and magenta colored).

124 The  $R_s$ ,  $C$  and  $R$  parameters are extracted as follows: first, on the  $R_p$ - $C_p$  response, the  $C_p$  value is  
 125 used for the  $C$  value, the low frequency  $R_p$  value is defined as the equivalent resistance  $R$  of the piezo-  
 126 cell and the  $R_s$  value is extracted from the high-frequency  $R_p$  measured response. This strategy is  
 127 proved to be physically relevant as the as-extracted  $R_s$ ,  $R$  and  $C$  values are then implemented in the  
 128 corresponding gain-phase response and the resulting simulated response is in excellent agreement with  
 129 the measured characteristics.

130 We then proceeded in the same way to extract  $R_s$ ,  $R$  and  $C$  values for all piezo-cell geometries  
 131 on two different chips. Values are listed below (Table 1) together with the theoretical  $C$  values for  
 132 comparison.

133 **Table 1:** Values of the series resistance for the electrical wiring ( $R_s$ ), the resistance of the piezo-layer  
 134 ( $R$ ) and the global capacitance of the piezo-cell and associated electrical wiring ( $C_{\text{meas}}$ ) extracted from  
 135 gain-phase measurements similar to Figure 7 and comparison with corresponding global capacitance

136 theoretical value ( $C_{\text{calculated}}$ )

| Cantilever/Bridge Chip |               |                     |                              |                                    | Membrane Chip |               |                     |                              |                                    |
|------------------------|---------------|---------------------|------------------------------|------------------------------------|---------------|---------------|---------------------|------------------------------|------------------------------------|
| Structure              | $R_s(\Omega)$ | $R(\text{G}\Omega)$ | $C_{\text{meas}}(\text{pF})$ | $C_{\text{calculated}}(\text{pF})$ | Structure     | $R_s(\Omega)$ | $R(\text{M}\Omega)$ | $C_{\text{meas}}(\text{pF})$ | $C_{\text{calculated}}(\text{pF})$ |
| S1                     | 60            | 50                  | 44                           | 66                                 | $S1_i$        | 45            | 30                  | 245                          | 239                                |
| S2                     | 70            | 50                  | 43                           | 59                                 | $S1_o$        | 35            | 4000                | 850                          | 718                                |
| S3                     | 60            | 50                  | 63                           | 77                                 | $S2_i$        | 30            | 120                 | 240                          | 238                                |
| S4                     | 60            | 50                  | 65                           | 78                                 | $S2_o$        | 18            | 5000                | 820                          | 718                                |
| S5                     | 50            | 50                  | 82                           | 99                                 | $S3_i$        | 23            | 800                 | 240                          | 239                                |
| S6                     | 60            | 50                  | 86                           | 107                                | $S3_o$        | 15            | 2000                | 830                          | 719                                |
| $S7_l$                 | 70            | 50                  | 43                           | 66                                 | $S4_i$        | 90            | 280                 | 55                           | 68                                 |
| $S7_r$                 | 70            | 50                  | 45                           | 68                                 | $S4_o$        | 40            | 500                 | 160                          | 164                                |
| $S8_l$                 | 60            | 50                  | 46                           | 71                                 | $S5_i$        | 60            | 700                 | 60                           | 82                                 |
| $S8_r$                 | 60            | 50                  | 43                           | 61                                 | $S5_o$        | 50            | 2500                | 165                          | 178                                |
| $S9_l$                 | 50            | 50                  | 69                           | 99                                 | $S6_i$        | 50            | 50                  | 65                           | 96                                 |
| $S9_r$                 | 50            | 50                  | 63                           | 78                                 | $S6_o$        | 50            | 1500                | 170                          | 191                                |
| $S10_l$                | 50            | 50                  | 70                           | 99                                 | $S7_i$        | 100           | 15000               | 11                           | 27                                 |

|                  |    |    |    |     |                 |     |       |    |    |
|------------------|----|----|----|-----|-----------------|-----|-------|----|----|
| S10 <sub>r</sub> | 50 | 50 | 62 | 78  | S7 <sub>o</sub> | 150 | 7000  | 16 | 33 |
| S11 <sub>i</sub> | 50 | 50 | 87 | 111 | S8 <sub>i</sub> | 150 | 15000 | 27 | 27 |
| S11 <sub>r</sub> | 45 | 50 | 82 | 99  | S8 <sub>o</sub> | 150 | 20000 | 27 | 33 |
| S12 <sub>i</sub> | 50 | 50 | 85 | 106 | S9 <sub>i</sub> | 150 | 20000 | 27 | 30 |
| S12 <sub>r</sub> | 45 | 50 | 85 | 104 | S9 <sub>o</sub> | 100 | 10000 | 28 | 34 |

137

138 A qualitative analysis of the Table 1 values reveals that:

- 139 - R systematically takes high resistance values (over tens of M $\Omega$ ), which is consistent with the  
140 high resistivities of the patterned sol-gel PZT ( $R_{pz}$ ) electrical properties used in this study and  
141 may include the leakage substrate resistive effects;
- 142 -  $R_s$  ranges from 15 $\Omega$  to 150 $\Omega$ , which is consistent with the series resistances values of the  
143 metallization measured on the Ti/Pt/Au stacks used to connect on-chip devices, resistive  
144 contact effects and bonding effects;
- 145 - The measured C values are of the same order of magnitude as the calculated values, but are  
146 not identical. This confirms the impact of the on-chip electrical wiring on the capacitive  
147 behavior of the piezo-cell. The influence of the wiring on the measured capacitance becomes  
148 progressively smaller for larger electrode areas on the PZT.

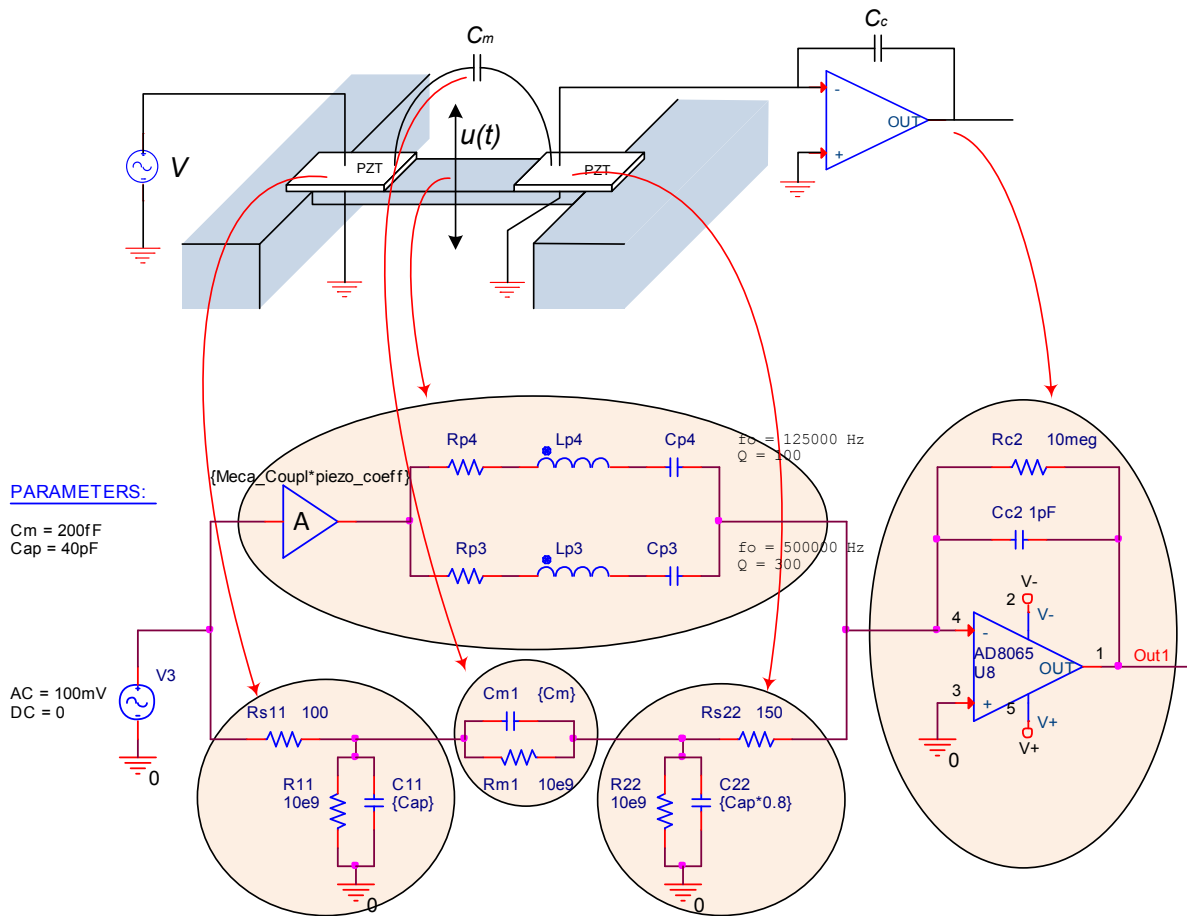
149 **Actuation and sensing strategies: Minimizing the impact of on-chip, design dependent parasitic**  
150 **capacitive effects**

151 The generic equivalent electrical model of a piezo-cell ( $R_s$ , R, C) can be subsequently  
152 implemented in piezoelectric transduction schemes [4, 7, 15, 16] in order to assess the configuration  
153 that minimizes the impact of parasitic capacitance on the actuation and sensing performance at the  
154 device level. In the present section, we will discuss two widely used actuation and sensing strategies  
155 and comment on the limitations imposed by parasitic effects inherent to silicon chip design. The first  
156 is the “*duo-piezo-cell structure*” which includes two separated piezo-cells on a single MEMS  
157 resonator, one dedicated to the actuation and the other to the detection. This is often achieved using  
158 clamped-clamped structures, such as bridges or membranes. The second is the “*mono-piezo-cell*”

159 *structure*” where the MEMS resonator needs only one piezo-cell. A second identical unreleased piezo-  
 160 cell is placed next to the previous one to be used as reference.

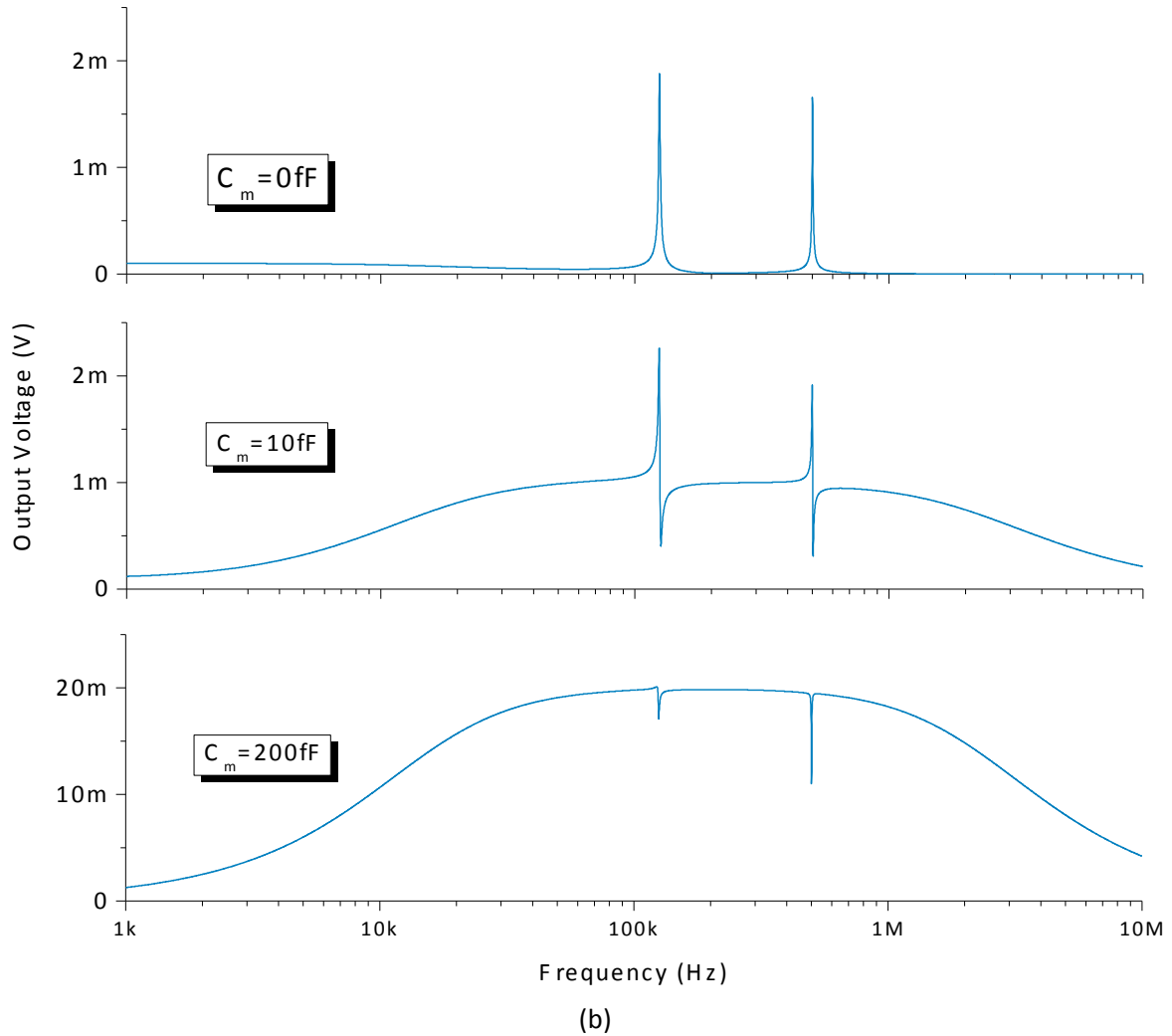
161 **The “duo-piezo-cell structure”**

162 Figure 3.(a) depicts a clamped-clamped resonator bearing two piezo-cells, one of which is used  
 163 for actuation, while the other is intended for sensing purposes. The electrical charges generated by the  
 164 sensing piezo-cell can be written as  $q(t) = CV_{sense} - xu(t)$  where  $C$  takes into account the  
 165 piezoelectric film and the associated on-chip electrical wiring capacitances,  $x$  is a transduction  
 166 coefficient ( $C/m$ ) and  $u(t)$  is the out-of-plane mechanical displacement of the beam. In this specific  
 167 configuration,  $V_{sense}$  is set to zero, which means that at the output of the charge amplifier,  $V_{out} = \frac{xu(t)}{C_c}$   
 168 where  $C_c$  is the feedback capacitor of the charge amplifier.



169  
 170

171 (a)



172  
173

174 **Figure 3:** (a) Schematic and behavioral modeling of a clamped-clamped beam with piezoelectric  
 175 integrated actuation/sensing piezo-cells. (b) Simulated  $V_{out}(V)$  at the output of the charge amplifier as a  
 176 function of frequency for three different values of mutual capacitance  $C_m$

177 In order to assess the global electrical behavior of the duo-piezo-cell configuration, an equivalent  
 178 electrical model for the device shown in Figure 3.(a) scheme was implemented and run using a PSpice  
 179 simulator. To model the experimental data, two resonant modes of the clamped-clamped beam were  
 180 represented by two  $RLC$  equivalent circuits where the gain  $A$  corresponds to the electromechanical  
 181 transduction coefficient. The electrical response is simulated on a 1kHz – 10MHz frequency range with  
 182 a 100mV excitation amplitude. In addition, the mutual capacitance ( $C_m$ ) between the two piezo-cells  
 183 was considered to assess the impact of this supplementary parasitic element on the global electrical

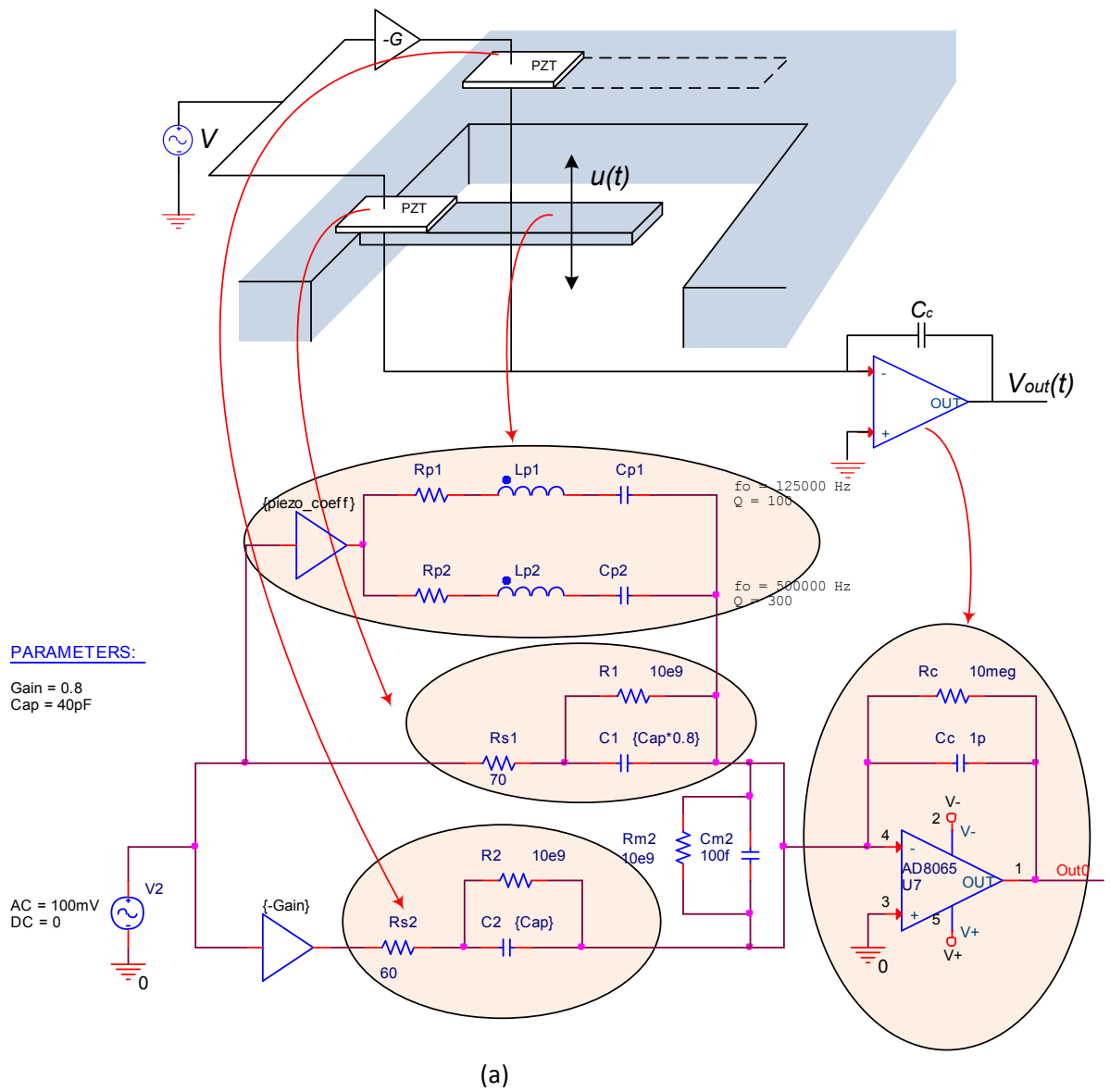
184 behavior of the resonator. A large resistance  $R_m$  (of order  $1G\Omega$ ) was added to account for surface  
 185 leakage currents between the two piezo-cells. Practically, this would describe finite leakages  
 186 associated with environmental conditions such as moisture, or surface defects on the chip. For  
 187 simplicity, the finite ac field dependence of the permittivity of the PZT films [17] was neglected. The  
 188 simulation result for three different values of  $C_m$  (0, 10fF and 200fF) is presented in Figure 3.(b).

189 For the low frequency range (*i.e.* below the cutoff frequency of the charge amplifier feedback  
 190 filter) the output charge amplifier voltage is given by the ratio of the feedback resistance of the charge  
 191 amplifier and  $R_m$ , such as  $V_{out} = \frac{R_{c2}}{R_m} V_{in}$ . For frequencies above the cutoff frequency, the influence of  
 192 the mutual capacitance can be assessed by observing the modification of the shape of the resonant  
 193 frequency peaks. For instance, in Figure 3.(b), in the case of the 200 fF value for  $C_m$ , the peaks invert.  
 194 At these frequencies, the magnitude of the plateau is given by  $V_{out} = \frac{C_m}{C_c} V_{in}$ . Thus, these parasitic  
 195 effects result from the influence of  $C_m$  and they cannot be avoided. The main advantage of a duo-  
 196 piezo-cell actuation/sensing scheme is the suppression of the effect of the static capacitance of the  
 197 sensing piezo-cell. However, the model demonstrates that this comes at a price of considerable impact  
 198 of the mutual capacitance on the peak shape. This effect becomes increasingly important as the  
 199 dimensions of the resonator shrink, as will be demonstrated in the experimental validation section of  
 200 this work.

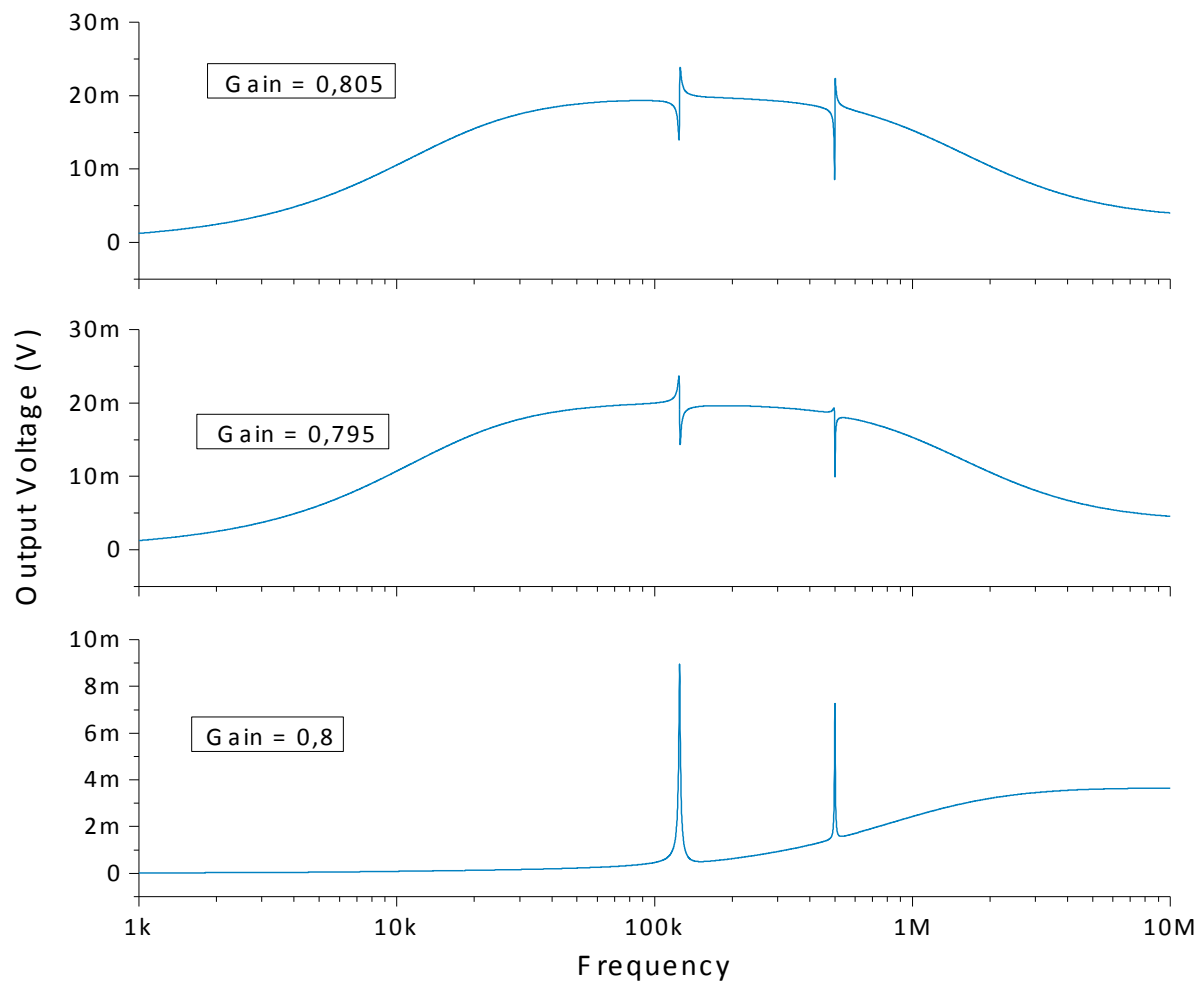
### 201 **The “mono-piezo-cell structure”**

202 Figure 4.(a) depicts a clamped-free resonator bearing one piezo-cell used for actuation or  
 203 sensing while a second remote piezo-cell is used as a reference capacitor. Comparable schemes have  
 204 been used since Lee et al.’s seminal work [4] proposing the first atomic force microscope, where the  
 205 optical detection scheme was replaced by an equivalent piezoelectric one. In this case, the charge  
 206 amplifier voltage is given by  $V_{out}(t) = \frac{(GC_{p2}-C_{p1})V+Xu(t)}{C_c}$  where  $C_{p1}$  and  $C_{p2}$ , respectively, account for  
 207 the piezoelectric film and the associated on-chip electrical wiring capacitances for each of the piezo-  
 208 cells. The gain  $G$  allows the piezo-cells to be balanced, so that after tuning  $G$ ,  $V_{out}(t) = \frac{xu(t)}{C_c}$ .

209           In order to assess the global electrical behavior of the mono-piezo-cell configuration, the  
210 equivalent electrical model for the device shown in Figure 4.(a) was implemented using a PSpice  
211 simulator. Two resonant modes of the clamped-free beam (the same as for the previous case) were  
212 represented by the resonances of two *RLC* equivalent circuits. In this configuration, the mutual  
213 capacitance between the piezo-cells has no effect on the output. Moreover, this design allows  
214 cancellation of the mutual capacitance due to the distance between the piezo-cells. The piezo-cells'  
215 capacitances values intentionally differ by 20% in this example in order to assess the role of  
216 fabrication variations on the global electrical behavior of the resonator, where  $G = 0.8$  cancels the  
217 20% difference between  $C_{p1}$  and  $C_{p2}$ . The simulation result of slight variations of the gain around its  
218 optimal value ( $G$  being respectively equal to 0.795, 0.8 and 0.805) is shown in Figure 4.(b):



219  
220



221

222

(b)

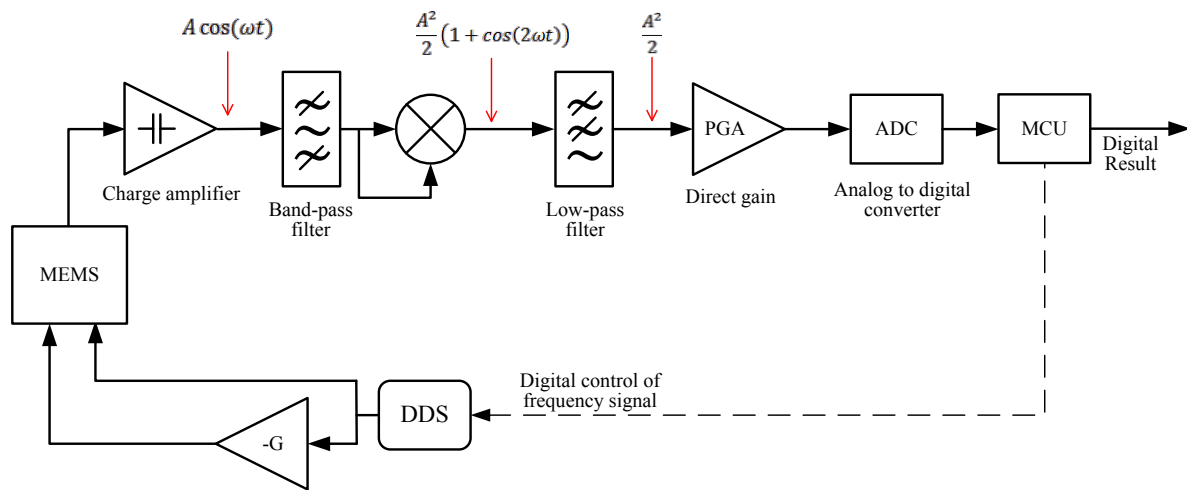
223 Figure 4: Schematics and behavioral modeling of a clamped-free beam with a single actuation/sensing  
 224 piezo-cell with a remote reference piezo-cell, which in this specific configuration remains unreleased  
 225 from the substrate; (b) Simulated  $V_{out}$ (V) at the output of the charge amplifier as a function of  
 226 frequency for three different values of balance gain  $G$

227 The simulation was performed for a  $S_2$  cantilever (see Supplementary Information file) with a  
 228 static equivalent capacitance of 40pF. The generated charge value from the released piezo-cell is equal  
 229 to 3.2pC compared to 4pC generated by the reference piezo-cell because of the 20% difference of  
 230 static capacitances. It is clearly seen from Figure 4.(b) that a compensation gain equal to 0.8 perfectly  
 231 balances the charges of both piezo-cells. A much cleaner resonant characteristic also results from

232 appropriate compensation of the static capacitances. A slight detuning of  $G$  to 0.795 or 0.805  
 233 immediately unbalances the piezo-cells compensation and subsequently produces residual  
 234 corresponding charges of 20fC which increase the off-resonance voltage level to 20mV and hence  
 235 dramatically impact the resonance shapes. Thus, for such an actuation/sensing scheme where the  
 236 mutual capacitance effects are canceled by design, the compensation of static capacitance is key to  
 237 obtain close-to-Lorentzian shaped resonance responses.

238 **Sensing specific electronics set-up and validation**

239 To experimentally confirm the effects of the mutual capacitance and of capacitive variations as  
 240 described in the previous sections, an electronics set-up was designed and constructed as illustrated in  
 241 Figure 5.



242  
243

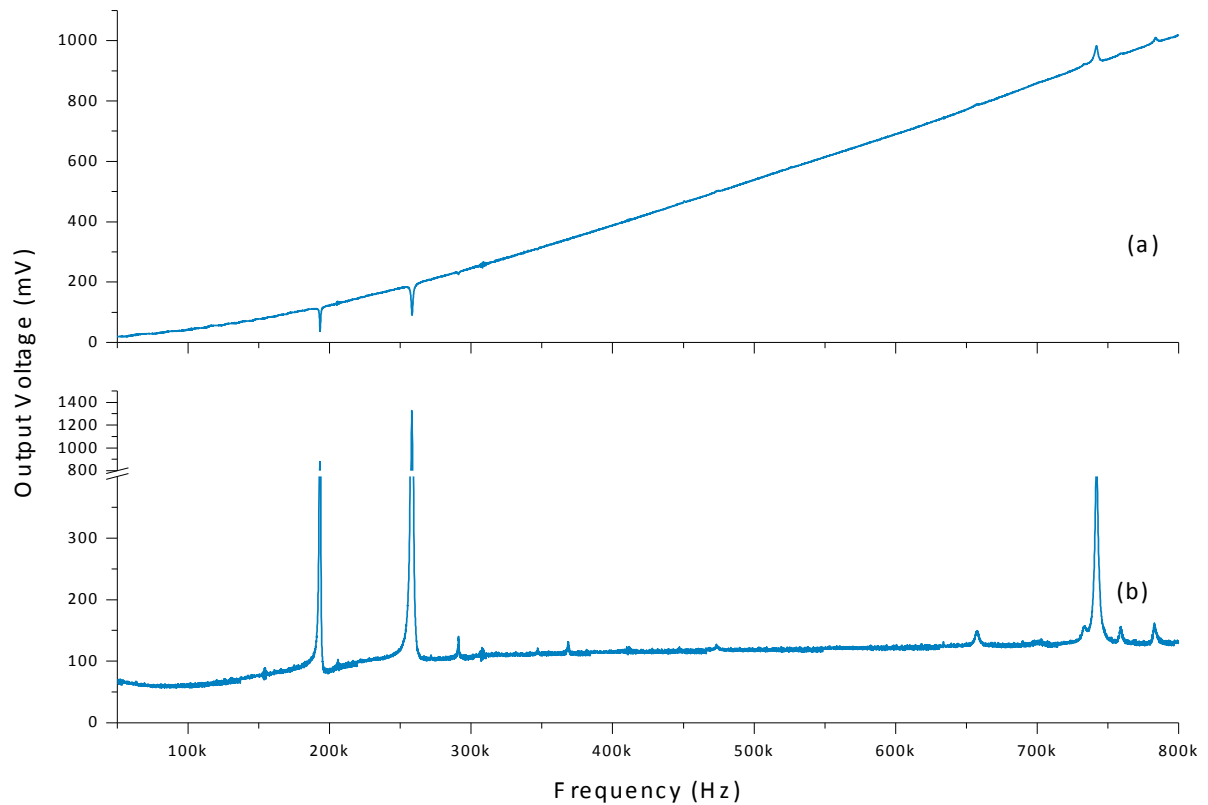
244 Figure 5: Schematic of the electronic set-up for piezo-MEMS actuation/sensing purposes.  $A$  is the  
 245 amplification factor, PGA stands for Programmable Gain Array, ADC is the Analog-to-Digital  
 246 Converter used to drive the microcontroller unit (MCU) and DDS is the Direct Digital Synthesizer.

247 A sinusoidal voltage of constant amplitude (10mV-4V) is applied to the piezo-cells for actuation  
 248 by a Direct Digital Synthesizer (AD9832, Analog Device, USA). The same signal may be fed through  
 249 a negative gain amplifier and subsequently applied to the piezo-cells used for compensation (in mono-  
 250 piezo-cell configuration). The piezo-MEMS output signal is then amplified by a charge amplifier (1

251 V/pC) and fed through a wide band-pass filter (10 kHz-2 MHz) to eliminate low frequency and digital  
252 noise. The signal is then multiplied by itself and low-band filtered to obtain a DC signal corresponding  
253 to its amplitude at a given frequency. This square of the signal is amplified by a settable gain (called  
254 the direct gain). The resulting analog signal is digitized to perform averaging, digital feedback for the  
255 frequency excitation, search for resonance modes in a given frequency band, calculation of the quality  
256 factor, and calculation and driving of the optimal direct gain. Data were sent through a USB  
257 (Universal Serial Bus) to a PC (Personal Computer) with a custom GUI (Graphical **User** Interface).  
258 Further actions can be performed subsequently, including: control and setting of the electronic card,  
259 acquisition of wide spectrum response, display of specific resonant modes with associated quality  
260 factors assessment, monitoring of a specific resonant mode, etc.

261         The importance of mutual capacitance effects is amplified when the actuation and sensing  
262 piezo-cells are on the same resonating structure. This configuration is met in the case of the circular  
263 membranes. The first spectrum in Figure 6 represents the effect of the mutual capacitance on the  
264 electrical dynamic response of a membrane (structure  $S_1$  in Figure S3, on the membrane chip). A  
265 30mV voltage is used to actuate the membrane on its inner electrode (the  $S_{1i}$  piezo-cell) while sensing  
266 is performed using the outer electrode (structure  $S_{1o}$  piezo-cell). It is worth noting that in Fig. 6(a) the  
267 voltage response presents inverted resonant peaks. In contrast, the mutual capacitance is eliminated  
268 when a remote piezo-cell (say,  $S_{40}$ ) on the same chip, is used for sensing.

269



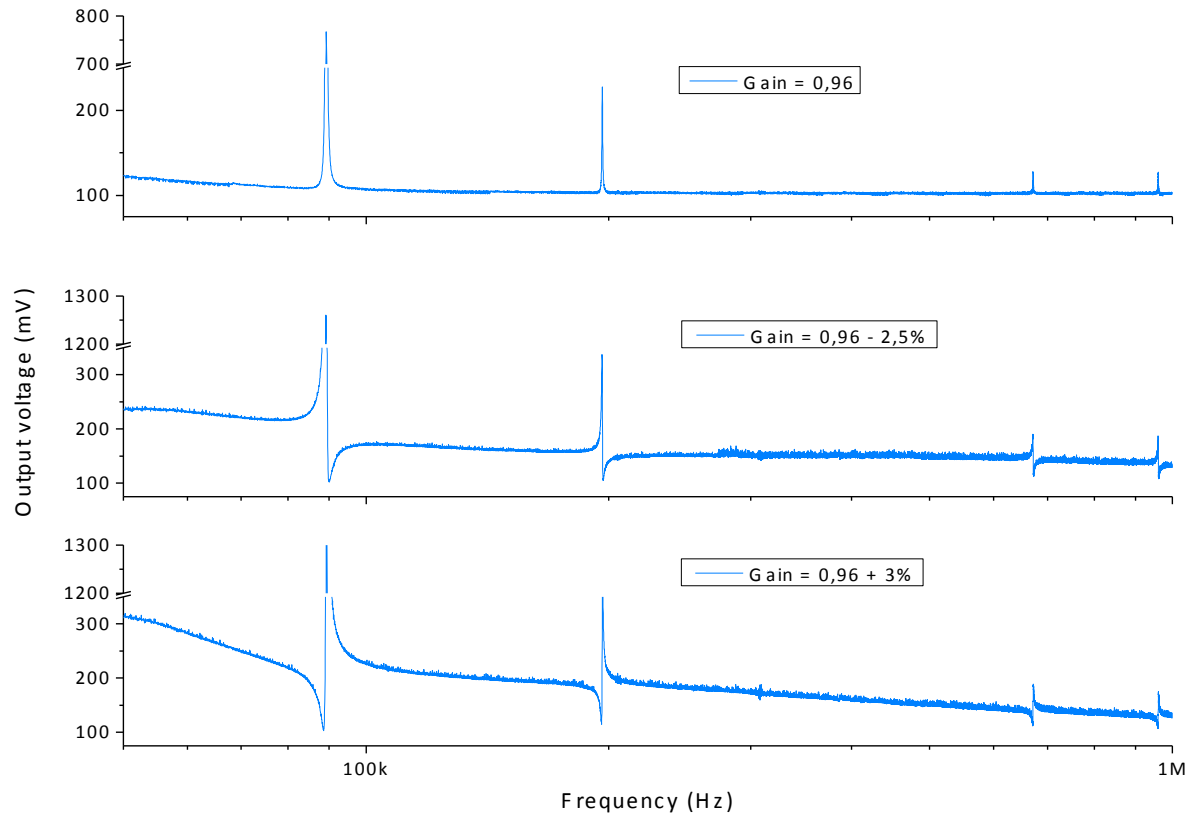
270  
271

272 Figure 6: Experimental responses of a piezoelectrically actuated/sensed membrane using (a) separated  
273 piezo-cells on one membrane for actuation and sensing purposes and (b) one single piezo-cell on the  
274 membrane balanced with respect to a similar piezo-cell located on a different membrane.

275 The effect of the mutual capacitance is emphasized by the inverted resonance shapes (Figure  
276 6.a). Once this effect is suppressed by the use of the “mono-piezo-cell” scheme, the dynamic response  
277 of the micromembrane becomes Lorentzian-shaped (Figure 6.b).

278 Making use of the same “mono-piezo-cell” configuration, a clamped-free beam bearing a single  
279 piezo-cell for both actuation/sensing purposes (e. g. structure  $S_3$  in Figure S3) was excited using a  
280 40mV voltage. Sensing was done with a piezo-cell reference on a neighboring bridge that was  
281 immobilized using a photoresist drop. Three resonant spectra were recorded (Figure 7) with  
282 compensation gain values set such that the piezo-cells were either perfectly balanced or up to 3%  
283 different.

284



285  
286

287 Figure 7: Experimental dynamic responses of a piezoelectrically actuated/sensed cantilever bearing a  
 288 single piezo-cell. Measurements were performed with respect to a motionless reference piezo-cell by  
 289 setting gain values used to compensate the differences between the piezo-cells such as they are either  
 290 up to 3% unbalanced (*b,c*) or perfectly balanced (*a*).

291 As predicted by the simulations of the mono-piezo-cell configuration, when the gain is set such  
 292 that both piezo-cells are perfectly compensated, the resonant peaks are close to Lorentzian-shaped  
 293 dynamic responses. Good agreement is achieved between the experimentally observed changes in the  
 294 shapes of the resonant peaks and the corresponding simulated behavior (see Figure 4.b). This enables  
 295 full control of the compensation once the first measurements are collected.

## 296 Conclusions

297 Collective fabrication of different geometries of microresonators (cantilevers, bridges and  
 298 membranes) bearing piezoelectric film for actuation/sensing purposes on the same wafer has been

299 done in order to devise design rules that best exploit the capabilities of the integrated piezoelectric thin  
300 films, while avoiding parasitic effects inherent to the integration at the micro-scale. Three main  
301 parasitic effects, namely the electrical wiring capacitance, the mutual capacitance between  
302 actuation/sensing piezo-cells and variations in the capacitance of the actuation/sensing piezo-cells,  
303 have been identified, modeled and experimentally investigated. Strategies to minimize their impact on  
304 the resonant behavior of the piezo-MEMS were also discussed.

305 An electrical model of a piezo-cell consisting of piezoelectric thin film sandwiched between two  
306 metallic electrodes was considered in order to systematically assess the role of the associated on-chip  
307 electrical network. Though this kind of consideration is a basic rule for microelectronics designers, it  
308 is often neglected in design of MEMS systems; this, in turn, may induce errors of interpretation of  
309 signals from the piezoelectric sensing piezo-cells.

310 When two independent piezo-cells are co-hosted on the same microscale resonator, mutual  
311 capacitance between the piezo-cells induces parasitic effects that influence the net piezo-MEMS  
312 electrical behavior. We have proven by simulation that fF-level mutual capacitances may considerably  
313 affect the Lorentzian shape of the resonant peaks. It was shown experimentally that on a  
314 micromembrane geometry bearing both actuation/sensing piezo-cells, use of a remote, motionless  
315 piezo-cell as a reference eliminates this problem.

316 Finally, the compensation of parasitic effects via a reference, unreleased piezo-cell is effective  
317 only if its capacitance value is identical to that of the active piezo-cell. This type of capacitive  
318 compensation scheme can be obtained by finely tuning the gain of the amplifier whose output voltage  
319 drives the reference piezo-cell.

320 Hence, it is of paramount importance for MEMS designers to have a holistic approach when  
321 dealing with actuation and sensing capabilities integrated at the device level. This is especially true  
322 when the measured electrical charge levels reflect the device motion and when the dimensions of the  
323 devices are on the micron scale. This kind of considerations will become progressively more important  
324 with the development of nano-electromechanical systems integrating actuation/sensing capabilities.

325 **Acknowledgements**

326 This publication was supported by the Pennsylvania State University Materials Research Institute  
327 Nanofabrication Lab and the National Science Foundation Cooperative Agreement No. ECS-0335765.  
328 The French National Agency for Research (program ANR/PNANO 2008, project NEMSPIEZO  
329 “ANR-08-NANO-015”) is gratefully acknowledged for financial support.

330

331 **References**

332 [1] P. Muralt, J. Am. Chem. Soc. 91 (2008) 1385-1396

333

334 [2] S. Trolier-McKinstry, F. Griggio, C. Yaeger, P. Jousse, D. Zhao, S. S. N. Bharadwaja, T. N.  
335 Jackson, S. Jesse, S. V. Kalinin and K. Wasa, IEEE Trans. Ultrason. Ferroelectr. Freq. Control 58  
336 (2011) 1782-1792

337

338 [3] P. Muralt, R. G. Polcawich and S. Trolier-McKinstry, MRS Bull. 34 (2009) 658-664

339

340 [4] C. Lee, T. Itoh and T. Suga, Sens. Actuators A 72 (1999) 179-188

341

342 [5] E. K. Hong, S. Trolier-McKinstry, R. L. Smith, S. V. Krishnaswamy and C. B. Freidhoff, J.  
343 Microelectromech. Syst. 15 (2006) 832-839

344

345 [6] J. D. Adams, L. Manning, B. Rogers, M. Jones and S. C. Minne, Sens. Actuators A 121 (2005)  
346 262-266

347

348 [7] L. Nicu, M. Guirardel, F. Chambosse, P. Rougerie, S. Hinh, E. Trevisiol, J.-M. Francois, J.-P.  
349 Majoral, A.-M. Caminade, E. Cattan and C. Bergaud, *Sens. Actuators B* 110 (2005) 125-136  
350

351 [8] V. Koval, S. S. N. Bharadwaja, M. Li, T. S. Mayer and S. Trolier-McKinstry, *Solid State Comm.*  
352 151 (2011) 1990-1993  
353

354 [9] H.A.C. Tilmans, *J. Micromech. Microeng.* 6 (1996) 157-176.  
355

356 [10] S. Horowitz, T. Nishida, L. Cattafesta and M. Sheplak, *J. Acoust. Soc. Am.* 122 (2007) 3428-  
357 3436.  
358

359 [11] B. A. Griffin, M. D. Williams, C. S. Coffman and M. Sheplak, *J. Microelectromech. Syst.* 20  
360 (2011) 476-486.  
361

362 [12] M. D. Williams, B. A. Griffin, T. N. Reagan, J. R. Underbrink and M. Sheplak, *J.*  
363 *Microelectromech. Syst.* 21 (2012) 270-282.  
364

365 [13] G. K. Ho, R. Abdolvand, A. Sivapurapu, S. Humad and F. Ayazi, *J. Microelectromech. Syst.* 17  
366 (2008) 512-520.  
367

368 [14] R. A. Wolf and S. Trolier-McKinstry, *J. Appl. Phys.* 95 (2004) 1397-1406  
369

370 [15] D. L. DeVoe, *Sens. Actuators A* 88 (2001) 263-272  
371

372 [16] C. Ayela, T. Alava, D. Lagrange, D. Remiens, C. Soyer, T. Ondarcuhu, A. Greve and L. Nicu,  
373 *IEEE Sensors J.* 8 (2008) 210-217

374

375 [17] N. Bassiri Gharb, I. Fujii, E. Hong, S. Trolier-McKinstry, D. V. Taylor and D. Damjanovic, J.

376 Electroceramics 19 (2007) 47 - 65

377

378